Journal of Materials Chemistry A

PAPER

View Article Online
View Journal | View Issue

Cite this: J. Mater. Chem. A, 2016, 4, 7781

Sodium chloride-assisted green synthesis of a 3D Fe–N–C hybrid as a highly active electrocatalyst for the oxygen reduction reaction†

Yun Zhang,[ab] Lin-Bo Huang,[ac] Wen-Jie Jiang,[ac] Xing Zhang,[ac] Yu-Yun Chen,[a] Zidong Wei,*[b] Li-Jun Wan[ac] and Jin-Song Hu*[ac]

Received 25th February 2016
Accepted 4th April 2016

DOI: 10.1039/c6ta01655c

www.rsc.org/MaterialsA

To promote the oxygen reduction reaction (ORR) on a non-precious-metal catalyst, integrating two-dimensional (2D) nanosheets and one-dimensional (1D) nanotubes in one catalyst is considered as one of the desirable approaches since this hybrid architecture can host more useful active sites and enhance mass/electron transfer. Herein, we demonstrated a sodium chloride-assisted strategy for the *in situ* synthesis of a three-dimensional (3D) hybrid of carbon nanosheets and nanotubes. The micrometer-scale sodium chloride (NaCl) crystal acted as a recyclable skeleton to adsorb the precursors on its surfaces, which assisted the formation of micrometer-sized graphitic carbon nanosheets with nanometer thickness by the template effect during the pyrolysis, and iron-based nanocrystals with a size of tens of nanometers by helping the distribution of iron sources and preventing their aggregation. The small iron-based nanocrystals favored the growth of long CNTs connected to carbon nanosheets and the outmigration of carbon atoms during the cooling process, which led to the formation of carbon-layer encapsulated metallic iron nanoparticles between the carbon nanosheets or inside the carbon nanotubes. Benefiting from these features, the developed hybrid exhibited a significantly enhanced electrocatalytic activity and durability for the ORR. The results may open up opportunities for exploring cost-effective high-performance electrocatalysts for energy applications.

Introduction

The oxygen reduction reaction is a critical step in determining the performance of clean and efficient next generation energy conversion devices, including fuel cells and metal–air batteries.[1–4] Since the electrochemical reduction of oxygen is kinetically sluggish in these devices, the development of electrocatalysts with sufficient ORR activity is crucial for the commercialization of these devices.[5,6] Although platinum-based materials exhibit excellent comprehensive performance in catalyzing the ORR, the prohibitive cost and scarcity of platinum hinder its application on a large scale.[7,8] Motivated by the economical and practical requirements, intensive efforts have therefore been devoted to exploring non-precious-metal catalysts (NPMCs) with an ORR activity close to, or even better than, that of the state-of-the-art Pt/C catalyst.[9–21]

Among various NPMCs, Fe–N–C-based materials are considered to be one of the most promising alternatives to Pt,[22–26] although the structure of the most active sites in these catalysts still remains elusive. Mukerjee *et al.* attributed the majority of the ORR activity of their Fe–N–C catalysts to the N-doped carbon structure instead of Fe or Fe–N_x coordination.[27] Jaouen *et al.* discovered the existence of porphyrin-like FeN_4C_{12} moieties in their Fe–N–C catalysts free or almost free of Fe crystalline structures and demonstrated that such moieties catalyzed the ORR through the 4-electron process.[28] They also found that the highly basic N-groups could enhance the ORR activity of FeN_4C_{12} moieties. Furthermore, many studies reported that the metal-based sites dominated the activity of Fe–N–C NPMCs.[29–31] Although the exact nature of active sites in Fe–N–C catalysts is still debatable, some experimental and theoretical results imply that iron clusters or nanoparticles can significantly enhance the electrocatalytic ORR activity of nitrogen doped carbon materials since the potential electron transfer from Fe-based nanoparticles to the N-doped carbon shells modified their electronic structure and decreased the local work function.[24,26] Recently, we revealed that Fe/Fe_3C nanocrystals could boost the electrocatalytic activity of Fe–N_x active sites for the ORR, leading to highly active Fe–N–C

[a]Beijing National Laboratory for Molecular Sciences, Key Laboratory of Molecular Nanostructure and Nanotechnology, Institute of Chemistry, Chinese Academy of Science, 2 North first Street, Zhongguancun, Beijing 100190, China. E-mail: hujs@iccas.ac.cn

[b]Chongqing Key Laboratory of Chemical Process for Clean Energy and Resource Utilization, Institution School of Chemistry and Chemical Engineering, Chongqing University, Shapingba 174, Chongqing 400044, China. E-mail: zdwei@cqu.edu.cn

[c]University of Chinese Academy of Science, Beijing 100049, China

† Electronic supplementary information (ESI) available: Fig. S1–S12 and Table S1. See DOI: 10.1039/c6ta01655c

catalysts.[32] Based on the profound understanding of catalytic centers, nanostructuring catalysts to have abundant highly catalytically active sites and favor both electron and mass transfer is an effective way to develop a high-performance ORR catalyst. The 3D doped carbon hybrid of graphitic carbon sheets (GCSs) and carbon nanotubes (CNTs) has been demonstrated to be one of the attractive options since GCSs are able to accommodate abundant active sites and CNTs improve the electron transportation and make the hybrid more accessible to the electrolyte.[33–37] However, developing a facile and easily scalable approach to prepare such a carbon hybrid and simultaneously integrate sufficient highly active sites for enhancing its performance is still desirable but challenging.

Here, we reported a simple sodium chloride (NaCl)-assisted pyrolysis approach for producing a 3D carbon hybrid of nanosheets and nanotubes which were integrated with abundant Fe–N_x structures and metallic iron-based nanocrystals as highly active centers for the ORR. Distinct from our previous work where the glucose shell pre-coated on CNTs was used to accommodate/create the Fe–N_x sites and metallic iron-based nanocrystals,[32] readily available and cheap small molecules without any additional pre-treatments were directly used herein as the carbon resources to achieve the distinctive 3D carbon hybrid with plenty of these active elements under the assistance of NaCl. Sodium chloride can be easily recycled *via* a recrystallization process, which makes the preparation cost-effective and easily scalable. It was found that NaCl dominated the formation of the GCS–CNT hybrid with an enlarged specific surface area (SSA) and porosity, and promoted the N-doping, the creation of the Fe–N_x configuration and the dispersion of iron-based nanocrystals. All these effects augment the highly active sites in the catalyst and make it exhibit catalytic activity and durability superior to those of the commercial Pt/C catalyst for the ORR.

Experimental section

Synthesis of Fe/Fe_3C@N–C–NaCl

In a typical synthesis, 0.61 g (1.5 mM) $Fe(NO_3)_3 \cdot 9H_2O$ (Alfa Aesar), 0.50 g glucose (Sinopharm Chemical Reagent Co., Ltd.), and 3.51 g NaCl (Sinopharm Chemical Reagent Co., Ltd.) were dissolved in 10 mL Milli-Q water to obtain a clear brown solution. The solution was then dried in a drying oven at 60 °C. The solid product and 1 g melamine (Sigma-Aldrich) were ground together. The gray mixture was then pyrolyzed at 800 °C for 120 min in a quartz tube under an argon atmosphere. This black product was washed with water. The black solid product was collected as the catalyst Fe/Fe_3C@N–C–NaCl. The aqueous solution was recrystallized to recycle NaCl.

Synthesis of control catalysts

Fe_3C@N–C was prepared in parallel by the same method as that for Fe/Fe_3C@N–C–NaCl except for no addition of NaCl. Other control catalysts were prepared in parallel by the same method as that for Fe/Fe_3C@N–C–NaCl except for no addition of melamine, glucose, or iron, respectively.

Characterization

The optical images were taken on an optical microscope (ECLIPSE LV150N, Nikon). The morphologies of all materials were investigated by using a scanning electron microscope (JSM 6701, JEOL, Japan) equipped with an energy dispersive spectroscopy (EDS) detector, and a transmission electron microscope (JEM-2100F, JEOL, Japan) operating at an accelerating voltage of 200 kV. X-ray diffraction (XRD) experiments were carried out on a Rigaku D/Max-2500 diffractometer equipped with a Cu Kα1 radiation source (λ = 1.54056 Å, Rigaku Corporation, Tokyo, Japan). Raman spectra were recorded on a Thermo Scientific DXR (532 nm laser wavelength). X-ray photoelectron spectroscopy (XPS) spectra were recorded on a VG ESCALab220i-XL with a monochromatic Mg Kα source. Thermogravimetric-differential thermal analysis (TGA-DSC) was carried out on a Shimadzu DTG-60H instrument under a flow of air or argon with a temperature ramp of 10 °C min^{-1}. Nitrogen adsorption–desorption isotherms were measured on a Quadrasorb SI-MP at 77 K. The specific surface area was calculated by the Brunauer–Emmett–Teller (BET) method and the pore size distribution curves were calculated by the Density Functional Theory (DFT) method.

Electrochemical measurements

The electrocatalytic experiments were performed using a rotating ring-disk electrode rotator (RRDE-3A, ALS, Japan) connected to an electrochemical workstation (CHI 760E, ChenHua, Shanghai, China) at room temperature. All measurements were done with a standard three electrode cell system, consisting of a standard Ag/AgCl (3 M KCl solution) as the reference electrode, a Pt wire as the counter electrode, and a rotating ring disk electrode (RRDE, 4 mm in diameter) coated with each catalyst as the working electrode. Before the tests, the RRDE was mechanically polished prior to use with 0.5–0.7 μm and then with 0.03–0.05 μm alumina slurry to obtain a mirror-like surface, followed by washing with ethanol, and dried in air. To prepare the working electrode, 2 mg catalyst was first dispersed in 800 μL of ethanol under sonication for 15 min to form a homogeneous ink. Then, 30.2 μL ink was slowly loaded onto the clean surface of the RRDE and dried to achieve a catalyst loading of 600 μg cm^{-2}. After that, 2 μL nafion (0.5 wt%) solution was dropped onto the electrode surface. After drying under atmospheric conditions, the electrode was ready for the test. Commercial Johnson-Matthey Pt/C with 20 wt% Pt loading was used for comparison. Pt loading on the electrode was 25.5 μg cm^{-2}.

The four-electron selectivity of a catalyst was evaluated on the basis of H_2O_2 yield, which was calculated from the following equation:

$$H_2O_2\ (\%) = 200 \times \frac{I_R/N}{(I_R/N) + I_D}$$

The electron transfer number (n) was calculated from the following equation:

$$n = 4 \times \frac{I_D}{(I_R/N) + I_D}$$

where I_D and I_R are the disk and ring currents, respectively; N is the ring collection efficiency and is equal to 0.424.

Results and discussion

The typical procedure for the synthesis of the current catalyst (designated as Fe/Fe_3C@N–C–NaCl) is illustrated in Fig. 1a. In brief, sodium chloride, glucose and ferric nitrate were dissolved in water and dried, followed by mixing with melamine *via* grinding. The optical photos in Fig. 1b and c show that sodium chloride crystals change from colorless to yellowish after the adsorption of precursors. Energy dispersive spectroscopy (EDS) evidences the coexistence of elements Na, Cl, C, N, O, and Fe in the particles (Fig. S1†), indicating the incorporation of raw materials. The mixture was then pyrolyzed at 800 °C in an argon flow. As shown in Fig. 1c and d, the yellowish mixture was converted to a black one due to the pyrolysis of carbonaceous materials. After the removal of NaCl by simple water washing, the final black product with a collapsed morphology with a large amount of small particles (Fig. 1e) was collected as the final catalyst. No signals of Na and Cl in the X-ray photoelectron spectroscopy (XPS) spectrum (Fig. S2†) indicate that NaCl has been completely removed. The eliminated NaCl can be easily recycled *via* a recrystallization procedure for the next run as shown in the inset in Fig. 1a.

Thermogravimetric-differential thermal analysis (TGA-DTA) was carried out in an argon flow to investigate the pyrolysis process. As shown in Fig. S3,† an obvious endothermic peak appears in the range of 256–306 °C corresponding to a weight loss of 27.9 wt%, which can be ascribed to the sublimation and decomposition of glucose and melamine. As the temperature increased, the carbonization and graphitization occurred in the catalysis of Fe/Fe_3C nanoparticles.[38] Meanwhile, the *in situ* nitrogen doping was achieved with the decomposition of melamine.[39] When the temperature reached 803 °C, another sharp endothermal peak was observed, which should be due to the melting of NaCl.

The X-ray diffraction (XRD) pattern (Fig. 2a) of Fe/Fe_3C@N–C–NaCl shows a typical diffraction peak of graphitic carbon at about 26°, two distinct peaks at 44.67 and 65.02° corresponding to the cubic Fe (JCPDS no. 06-0696), and a set of small peaks including ones at 37.74, 44.99, 45.86, and 49.15°, which can be well attributed to the orthorhombic Fe_3C (JCPDS no. 35-0772). This result indicates that the product contains graphitic carbon, metallic Fe and Fe_3C. The much higher intensity of the diffraction peaks of metallic Fe *vs.* Fe_3C implies that the elemental iron mainly exists in the form of metallic Fe. In contrast, only graphitic carbon and orthorhombic Fe_3C phases were identified in the XRD pattern of Fe_3C@N–C (Fig. 2a) which was prepared by the same procedure as Fe/Fe_3C@N–C–NaCl except for no addition of NaCl.

The scanning electron microscopy (SEM) (Fig. 2b) and transmission electron microscopy (TEM) images (Fig. 2c) reveal that Fe/Fe_3C@N–C–NaCl is composed of a number of CNTs with a length of several microns and graphitic carbon nanosheets, which are connected together to form a hybrid of nanotubes and nanosheets. Such a 3D hybrid structure is expected to favor both electron transfer and mass transfer during the catalytic reaction. The zoom-in TEM image (Fig. 2d) clearly exhibits that the nanoparticles with a size of tens of nanometers with a darker contrast exist inside CNTs, which is consistent with the SEM observation (inset in Fig. 2d). The high resolution TEM (HRTEM) image (Fig. 2f) of these nanoparticles shows continuous lattice fringes in the dark part with a distance of 0.204 nm encapsulated inside carbon layers. This distance corresponds to

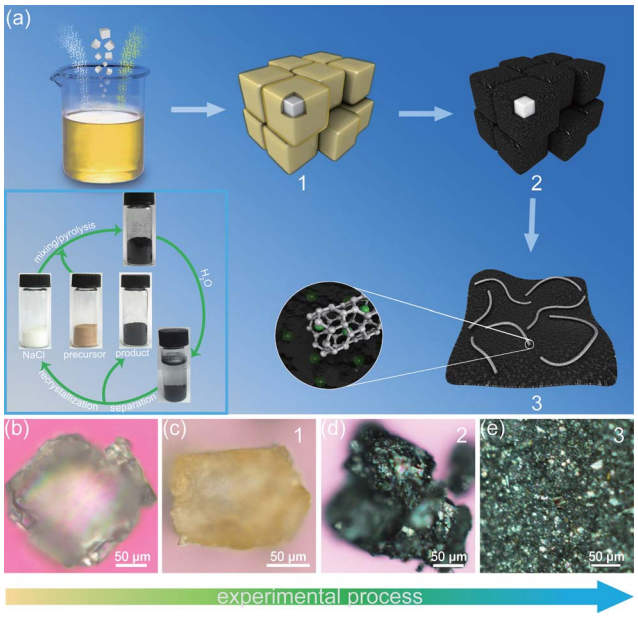

Fig. 1 (a) Schematic illustration of the preparation of Fe/Fe_3C@N–C–NaCl. (b–e) Optical photos of products at different stages: (b) pure NaCl crystal; (c) NaCl crystal with adsorbed precursors corresponding to intermediate product 1 in (a); (d) pyrolyzed product 2; (e) final catalyst after removal of NaCl corresponding to product 3.

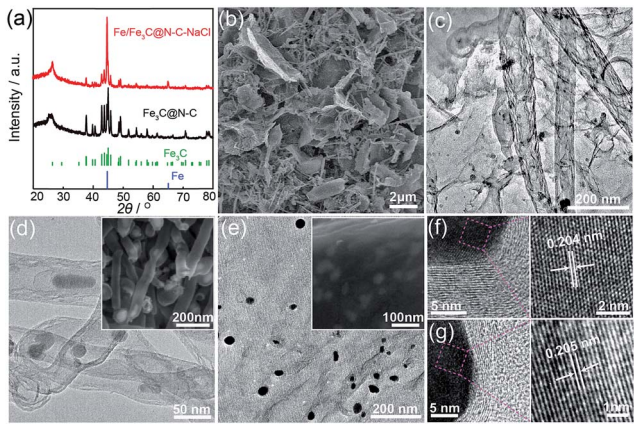

Fig. 2 (a) XRD patterns of Fe/Fe_3C@N–C–NaCl and Fe_3C@N–C. (b) SEM and (c) TEM images of Fe/Fe_3C@N–C–NaCl. TEM images of CNT (d) and GCS (e) in Fe/Fe_3C@N–C–NaCl. HRTEM images of nanoparticles in CNT (f) and GCS (g), respectively.

the (110) crystallographic planes of cubic Fe or (031) crystallographic planes of orthorhombic Fe_3C, indicating that these nanoparticles are single-crystalline Fe or Fe_3C nanocrystals. Moreover, similar nanocrystals are also observed on carbon nanosheets as shown in TEM images (Fig. 2e). The high magnification SEM image (inset in Fig. 2d) reveals that these nanoparticles are sandwiched between carbon layers. The HRTEM image indicates that the nanocrystals are encased by several carbon layers (Fig. 2g). In contrast, the control catalyst Fe_3C@N–C shows an irregular morphology with larger particles, sheets, and a small amount of short nanotubes (Fig. S4†). Therefore, it was believed that the adsorption of precursors onto the surfaces of micrometer-scale NaCl crystals (as shown in Fig. 1c) assisted the formation of micrometer-sized graphitic carbon nanosheets by the template effect during the pyrolysis. It also favored the distribution of iron sources and prevented their aggregation during the pyrolysis, which resulted in small iron-based nanocrystals with a size of tens of nanometers on carbon sheets instead of larger aggregates. The small size of these iron-based nanocrystals benefited the catalytic growth of long CNTs which were connected to carbon nanosheets forming a 3D hybrid structure, and the outmigration of carbon atoms during the cooling process which led to the formation of carbon-layer encapsulated metallic iron nanoparticles between the carbon nanosheets or inside the carbon nanotubes.

The BET SSA of both catalysts was determined by the nitrogen adsorption/desorption isotherm experiments (Fig. 3). The SSA of Fe/Fe_3C@N–C–NaCl was 192 $m^2\ g^{-1}$, much larger than 83 $m^2\ g^{-1}$ of Fe_3C@N–C (Fig. 3a). The pore size distribution analysis (Fig. 3b) shows that Fe/Fe_3C@N–C–NaCl has plenty of nanopores centered at 0.86 nm, 1.27 nm, and 5.3 nm with a total pore volume of 0.28 $cm^3\ g^{-1}$ (*vs.* 0.17 $cm^3\ g^{-1}$ for Fe_3C@N–C). HRTEM images confirm the existence of nanopores on the surface of catalysts (Fig. S5†). As reported, the larger amount of SSA and nanopores will assist in creating more catalytically active sites and make them accessible.[40–42] Moreover, the total iron content, determined by TGA under air atmosphere, is 28.05 wt% in Fe/Fe_3C@N–C–NaCl, which is slightly smaller than 30.27 wt% in Fe_3C@N–C (Fig. S6†), indicating that the introduction of NaCl reduces the weight loss during pyrolysis since Na-containing compounds can act as catalysts to promote the carbon conversion.[43,44] The surface iron content was estimated by XPS, which is only 0.22 at% for Fe/Fe_3C@N–C–NaCl and 0.25 at% for Fe_3C@N–C (Fig. S7†). These results corroborate the TEM and SEM observations that Fe/Fe_3C nanoparticles are inside the CNTs, or encased by carbon layers and sandwiched between carbon nanosheets. The total nitrogen calculated from XPS spectra is 3.13 at% for Fe/Fe_3C@N–C–NaCl, higher than 2.19 at% for Fe_3C@N–C (Fig. S2†). The above analyses disclose that NaCl assistance is effective in obtaining a catalyst with a larger SSA, pore volume, and high nitrogen content, which are favorable for enhancing the electrocatalytic activity of an ORR catalyst.

The chemical environment of nitrogen and iron in the catalysts was further analyzed by XPS and Raman spectroscopy and compared with that of iron(II) phthalocyanine (FePc), a standard reference compound with $Fe–N_4$ structure. As shown in Fig. 4a, the N1s signal of FePc shows two typical components: ~398.26 eV for C–N and ~399.46 eV for $Fe–N_x$.[45] The N1s signals of the present catalysts can be well deconvoluted into four typical components (~398.26 eV for C–N, ~399.46 eV for $Fe–N_x$, ~400.39 eV for quaternary-N, and ~401.53 eV for oxidized-N) as shown in Fig. 4a. The content of the $Fe–N_x$ configuration was calculated to be 1.34 at% in Fe/Fe_3C@N–C–NaCl *vs.* 0.53 at% in Fe_3C@N–C (Table S1†), indicating that the NaCl assistance promoted the formation of the $Fe–N_x$ configuration which could bring better ORR activity since the $Fe–N_x$ configuration has been reported to have highly active sites for ORR in previous studies.[28–32,46] Moreover, the $Fe–N_x$ configuration can be further corroborated by Raman spectra. Both Fe/Fe_3C@N–C–NaCl and Fe_3C@N–C exhibit Raman signals at 219.26 and 282.90 cm^{-1} (Fig. 4b), which match well with the ones of FePc and can be attributed to the vibrational modes involving Fe–N.[47]

The electrocatalytic activities of the catalysts were evaluated by linear sweep voltammetry (LSV) and compared with that of

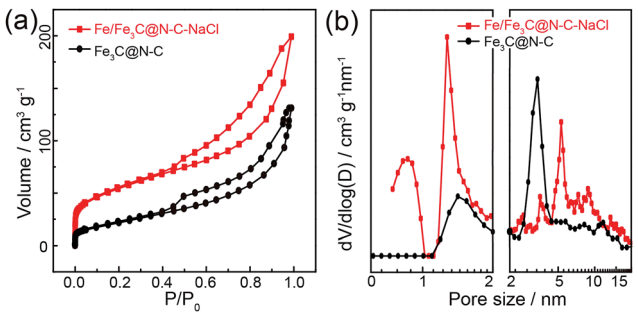

Fig. 3 (a) N_2 adsorption/desorption isotherms of Fe/Fe_3C@N–C–NaCl and Fe_3C@N–C. (b) The corresponding pore size distribution curves calculated from the desorption branches.

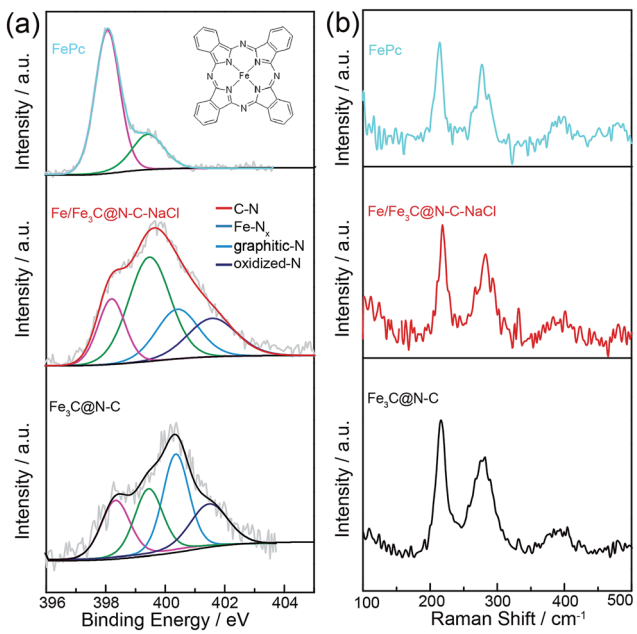

Fig. 4 (a) High-resolution N1s signals in XPS spectra and (b) Raman spectra of FePc, Fe/Fe_3C@N–C–NaCl and Fe_3C@N–C.

the commercial Johnson Matthey Pt/C catalyst (20 wt% Pt). As shown in Fig. 5a top, the control Fe_3C@N–C shows a moderate ORR activity with an on-set potential of 0.911 V (all potentials in the context are *versus* RHE) and a half-wave potential of 0.779 V while the Fe/Fe_3C@N–C–NaCl gives a more positive on-set potential (0.970 V) and a remarkably positively shifted half-wave potential (0.869 V), suggesting a much better ORR activity. This activity is also slightly higher than that of commercial Pt/C in terms of a 13 mV positively shifted half-wave potential. The same result can be obtained in cyclic voltammetry (CV) experiments where the Fe/Fe_3C@N–C–NaCl exhibits the most positive on-set potential and highest cathodic peak current (Fig. 5b), indicating its highest activity among three catalysts. Moreover, the RRDE experiments disclose that the H_2O_2 yield on Fe/Fe_3C@N–C–NaCl remains below 6.3% at all potentials, the lowest among all three catalysts (Fig. 5a bottom). This result implies that the electron-transfer number (n) of the ORR on Fe/Fe_3C@N–C–NaCl is over 3.9, which means that the reaction is dominated by a four-electron process (Fig. 5a middle). The Tafel slope was calculated to be 67 mV decade^{-1} for Fe/Fe_3C@N–C–NaCl, slightly smaller than 69 mV decade^{-1} of commercial Pt/C and significantly smaller than 80 mV decade^{-1} of Fe_3C@N–C, indicative of a good kinetic process for the ORR on Fe/Fe_3C@N–C–NaCl (Fig. 5c). The kinetic mass current of the Fe/Fe_3C@N–C–NaCl at 0.9 V is 2.79 A g^{-1}, which is larger than that of some Fe–N–C catalysts reported recently (such as 1.9 A g^{-1} reported by Rojas *et al.*),[48] but lower than that of our previous CNT-based Fe–N–C catalyst and some of other Fe–N–C catalysts.[32,49–51] Although this value is still lower than 9.97 A g^{-1} of Pt/C, it is in line with the DOE's target for NPMCs (with ORR mass activity 10 times lower than that of commercial Pt/C).

The stability of Fe/Fe_3C@N–C–NaCl in catalyzing the ORR was assessed by chronoamperometric measurements. As shown in Fig. 6a, 90.5% current remains for Fe/Fe_3C@N–C–NaCl after the 10 000 s test while Pt/C loses 56.4% of its initial current, indicating that the former delivered a much better durability than Pt/C. The durability of the Fe/Fe_3C@N–C–NaCl catalyst was further evaluated by cycling the potential between 0.6 and 1.0 V in oxygen-saturated 0.1 M KOH at 50 mV s^{-1}. As shown in Fig. S8,† after 5000 continuous cycles Fe/Fe_3C@N–C–NaCl shows no degradation in the on-set potential and a very slight shift of half-wave potential (8 mV), as well as a slight attenuation in diffusion-limited current density which is commonly observed in Pt/C and other electrocatalysts and could be due to the carbon erosion and the deterioration of the contact between catalysts and the electrode. In addition, its tolerance for methanol crossover was tested for the potential application in direct methanol fuel cells where methanol may pass across the membrane and thus deteriorate ORR catalysts (Fig. 6b). Fe/Fe_3C@N–C–NaCl exhibits no obvious change in the cathodic current after the addition of methanol into the electrolyte while Pt/C displays a significant methanol oxidation current, suggesting that the former demonstrated much better tolerance for methanol crossover.

In order to understand the high activity of Fe/Fe_3C@N–C–NaCl, three additional control catalysts were prepared by the same procedure except for no addition of melamine, glucose, or iron source, respectively. It was found that each of these starting materials influenced the morphology of the product besides NaCl. As shown in TEM images (Fig. S9†): (1) without melamine in the synthesis, the product is composed of carbon sheets and Fe-based nanoparticles most of which are not encased by carbon shells; (2) without glucose, the product consists of tube-like carbon and irregular Fe-based particles some of which are not covered by carbon; (3) without iron sources, the product is porous carbon nanosheets with a high SSA of 400 m^2 g^{-1} (Fig. S10a and b†). Therefore, it can be inferred that (1) glucose is essential for the formation of nanosheet-like structures, probably because it helped the adsorption of precursors onto the surfaces of NaCl crystals; (2) melamine and the iron source are essential for the formation of long carbon nanotubes since iron nanoparticles *in situ* formed in the pyrolysis can easily

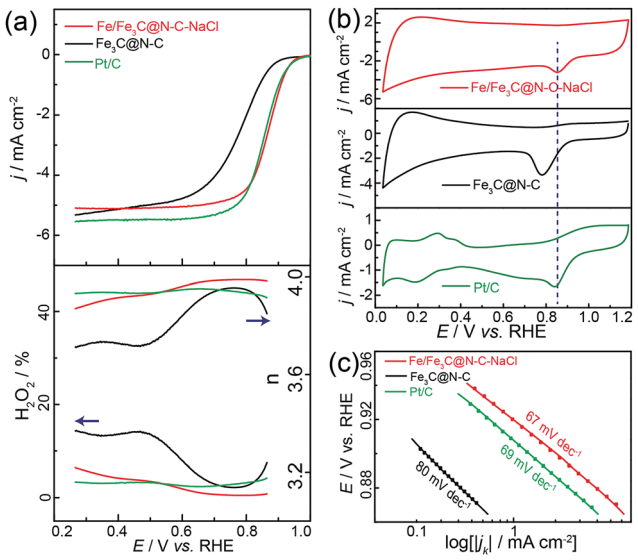

Fig. 5 (a) LSV curves of different catalysts (top), and the corresponding H_2O_2 yield (bottom) recorded at a scan rate of 10 mV s^{-1} and a rotation speed of 1600 rpm, and the calculated electron transfer number (middle). (b) CV curves of different catalysts recorded at a scan rate of 50 mV s^{-1}. (c) Tafel plots obtained from the RRDE measurements. All measurements were carried out in O_2-saturated 0.1 M KOH.

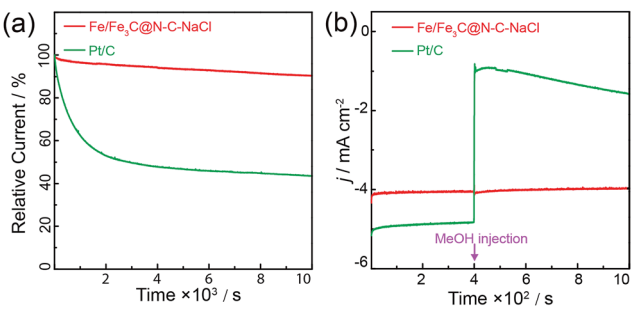

Fig. 6 (a) Relative current–time (i–t) chronoamperometric responses and (b) current–time (i–t) chronoamperometric responses of Fe/Fe_3C@N–C–NaCl and Pt/C. The arrow indicates the addition of methanol. All measurements were recorded at 0.764 V *vs.* RHE in O_2-saturated 0.1 M KOH solution.

catalyze the growth of carbon nanotubes at high temperature when nitrogen-containing organic compounds (melamine here) existed as carbon sources. Moreover, the XRD measurements indicate that the iron oxides exist in the product prepared without melamine or glucose, especially in the former, which is probably due to the partial oxidation of the exposed metallic Fe nanoparticles without carbon shells during the aqueous washing and drying process; the XRD pattern of the product prepared without iron sources shows only the features of carbon with a peak at about 26° (Fig. S11†).

The electrocatalytic performances of all control catalysts for the ORR were further measured *via* RRDE. As shown in Fig. 7a, the catalyst prepared without iron sources exhibits the worst performance although it has the largest SSA (400 m^2 g^{-1}) and highest nitrogen content (10.20 at%, Fig. S10c†). Both catalysts prepared without melamine or glucose show poor activity for the ORR, much lower than that of Fe/Fe_3C@N–C–NaCl. The H_2O_2 yield, CV curves and half-wave potentials and during the ORR present a consistent conclusion (Fig. 7a–c). Taking all these electrochemical measurements together, the results reveal that the coexistence of N-doping and Fe–N_x configuration is necessary for high ORR activity, and the metallic Fe nanocrystals and higher content of Fe–N_x configuration will enhance the electrocatalytic activity of this type of Fe–N–C catalyst.

It should be noted that the pyrolysis temperature and the amount of iron will also affect the ORR activities of catalysts. The polarization curves of catalysts prepared at different pyrolysis temperatures shown in Fig. S12a† indicate that the catalyst obtained at 800 °C exhibits a more positive on-set potential and half-wave potential, and thus better electrocatalytic activity for the ORR than the catalysts prepared at 700 or 900 °C. Moreover, as shown in Fig. S12b,† the polarization curves of catalysts with different iron contents show that the catalyst (1 mM Fe) gives a bit more positive on-set potential than the other two catalysts, but it shows the lowest diffusion current density. Therefore, we chose an iron content of 1.5 mM to prepare the above catalysts which display a suitable ORR activity in terms of both half-wave potential and diffusion current density.

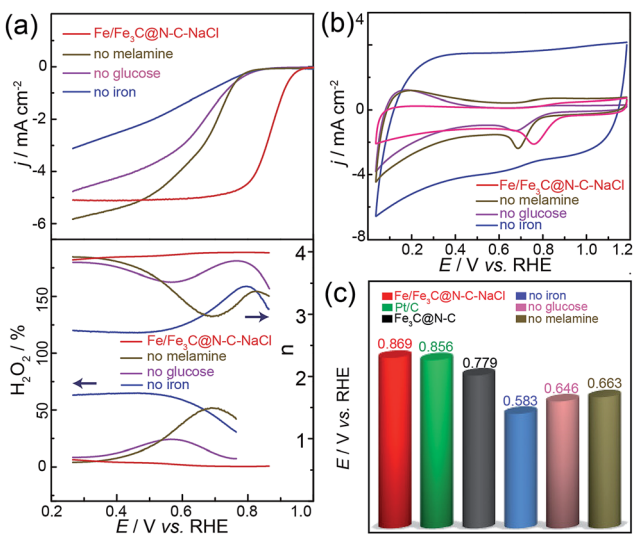

Fig. 7 (a) A comparison of LSV curves of control catalysts with those of Fe/Fe_3C@N–C–NaCl (top), and the corresponding H_2O_2 yield (bottom) recorded at a scan rate of 10 mV s^{-1} and a rotation speed of 1600 rpm, and the calculated electron transfer number (middle). (b) CV curves of different catalysts recorded at a scan rate of 50 mV s^{-1}. All measurements were carried out in O_2-saturated 0.1 M KOH. (c) A comparison of half-wave potentials of different catalysts.

Conclusions

In summary, a hybrid of carbon nanosheets and nanotubes hosting abundant Fe–N_x structures and metallic iron-based nanocrystals was developed by simple sodium chloride assisted pyrolysis. It was proved that NaCl helped to produce a high performance electrocatalyst in several ways: (1) rendering the 3D hybrid structure composed of nanosheets and nanotubes with an enlarged SSA and porosity for accommodating sufficient active sites and facilitating electron/mass transfer; (2) promoting N-doping and the formation of the Fe–N_x configuration; and (3) assisting in creating carbon-encased metallic Fe-based nanocrystals. As a result, the developed catalyst demonstrated a superior activity and durability for the ORR. This approach may inspire the mass production of new cost-effective and high-performance electrocatalysts for fuel cells and metal–air batteries.

Acknowledgements

We acknowledge the financial support from the National Key Project on Basic Research (2015CB932302, and 2012CB215500), the National Natural Science Foundation of China (21573249 and 21436003), and the Strategic Priority Research Program of the Chinese Academy of Sciences (Grant No. XDB12020100).

Notes and references

1 M. Winter and R. J. Brodd, *Chem. Rev.*, 2004, **104**, 4245–4270.
2 M. Armand and J.-M. Tarascon, *Nature*, 2008, **451**, 652–657.
3 Z.-L. Wang, D. Xu, J.-J. Xu and X.-B. Zhang, *Chem. Soc. Rev.*, 2014, **43**, 7746–7786.
4 A. Kumar, F. Ciucci, A. N. M, orozovska, S. V. Kalinin and S. Jesse, *Nat. Chem.*, 2011, **3**, 707–713.
5 Y. Zheng, Y. Jiao, M. Jaroniec, Y. Jin and S. Z. Qiao, *Small*, 2012, **8**, 3550–3566.
6 F. Cheng, J. Shen, B. Peng, Y. Pan, Z. Tao and J. Chen, *Nat. Chem.*, 2011, **3**, 79–84.
7 Z. Chen, D. Higgins, A. Yu, L. Zhang and J. Zhang, *Energy Environ. Sci.*, 2011, **4**, 3167–3192.
8 Q. Li, R. Cao, J. Cho and G. Wu, *Adv. Energy Mater.*, 2014, **4**, 1301415.
9 K. Gong, F. Du, Z. Xia, M. Durstock and L. Dai, *Science*, 2009, **323**, 760–764.
10 M. Lefèvre, E. Proietti, F. Jaouen and J.-P. Dodelet, *Science*, 2009, **324**, 71–74.
11 Y. Zheng, Y. Jiao, L. Ge, M. Jaroniec and S. Z. Qiao, *Angew. Chem., Int. Ed.*, 2013, **52**, 3110–3116.

12 Z. Yang, Z. Yao, G. Li, G. Fang, H. Nie, Z. Liu, X. Zhou, X. a. Chen and S. Huang, *ACS Nano*, 2012, **6**, 205–211.
13 G. Wu, K. L. More, C. M. Johnston and P. Zelenay, *Science*, 2011, **332**, 443–447.
14 J.-S. Lee, G. S. Park, H. I. Lee, S. T. Kim, R. Cao, M. Liu and J. Cho, *Nano Lett.*, 2011, **11**, 5362–5366.
15 S. Guo, S. Zhang, L. Wu and S. Sun, *Angew. Chem., Int. Ed.*, 2012, **51**, 11770–11773.
16 J. Liu, X. Sun, P. Song, Y. Zhang, W. Xing and W. Xu, *Adv. Mater.*, 2013, **25**, 6879–6883.
17 J. Tian, A. Morozan, M. T. Sougrati, M. Lefèvre, R. Chenitz, J.-P. Dodelet, D. Jones and F. Jaouen, *Angew. Chem., Int. Ed.*, 2013, **52**, 6867–6870.
18 Y. Zhang, W.-J. Jiang, L. Guo, X. Zhang, J.-S. Hu, Z. Wei and L.-J. Wan, *ACS Appl. Mater. Interfaces*, 2015, **7**, 11508–11515.
19 Y. Wang, Y. Nie, W. Ding, S. G. Chen, K. Xiong, X. Q. Qi, Y. Zhang, J. Wang and Z. D. Wei, *Chem. Commun.*, 2015, **51**, 8942–8945.
20 H. T. Chung, J. H. Won and P. Zelenay, *Nat. Commun.*, 2013, **4**, 1922.
21 R. Cao, R. Thapa, H. Kim, X. Xu, M. Gyu Kim, Q. Li, N. Park, M. Liu and J. Cho, *Nat. Commun.*, 2013, **4**, 2076.
22 Y. Hou, T. Huang, Z. Wen, S. Mao, S. Cui and J. Chen, *Adv. Energy Mater.*, 2014, **4**, 1400337.
23 Z. Wen, S. Ci, F. Zhang, X. Feng, S. Cui, S. Mao, S. Luo, Z. He and J. Chen, *Adv. Mater.*, 2012, **24**, 1399–1404.
24 Y. Hu, J. O. Jensen, W. Zhang, L. N. Cleemann, W. Xing, N. J. Bjerrum and Q. Li, *Angew. Chem., Int. Ed.*, 2014, **53**, 3675–3679.
25 K. Ai, Y. Liu, C. Ruan, L. Lu and G. Lu, *Adv. Mater.*, 2013, **25**, 998–1003.
26 D. Deng, L. Yu, X. Chen, G. Wang, L. Jin, X. Pan, J. Deng, G. Sun and X. Bao, *Angew. Chem. Int. Ed.*, 2013, **52**, 371–375.
27 K. Strickland, E. Miner, Q. Jia, U. Tylus, N. Ramaswamy, W. Liang, M.-T. Sougrati, F. Jaouen and S. Mukerjee, *Nat. Commun.*, 2015, **6**, 7343.
28 A. Zitolo, V. Goellner, V. Armel, M.-T. Sougrati, T. Mineva, L. Stievano, E. Fonda and F. Jaouen, *Nat. Mater.*, 2015, **14**, 937–942.
29 N. R. Sahraie, U. I. Kramm, J. Steinberg, Y. Zhang, A. Thomas, T. Reier, J.-P. Paraknowitsch and P. Strasser, *Nat. Commun.*, 2015, **6**, 8618.
30 Q. Jia, N. Ramaswamy, H. Hafiz, U. Tylus, K. Strickland, G. Wu, B. Barbiellini, A. Bansil, E. F. Holby, P. Zelenay and S. Mukerjee, *ACS Nano*, 2015, **9**, 12496–12505.
31 U. I. Kramm, I. Herrmann-Geppert, J. Behrends, K. Lips, S. Fiechter and P. Bogdanoff, *J. Am. Chem. Soc.*, 2016, **138**, 635–640.
32 W.-J. Jiang, L. Gu, L. Li, Y. Zhang, X. Zhang, L.-J. Zhang, J.-Q. Wang, J.-S. Hu, Z. Wei and L.-J. Wan, *J. Am. Chem. Soc.*, 2016, **138**, 3570–3578.
33 P. Chen, T.-Y. Xiao, Y.-H. Qian, S.-S. Li and S.-H. Yu, *Adv. Mater.*, 2013, **25**, 3192–3196.
34 Z. Jin, H. Nie, Z. Yang, J. Zhang, Z. Liu, X. Xu and S. Huang, *Nanoscale*, 2012, **4**, 6455–6460.
35 Y. Zhang, W.-J. Jiang, X. Zhang, L. Guo, J.-S. Hu, Z. Wei and L.-J. Wan, *Phys. Chem. Chem. Phys.*, 2014, **16**, 13605–13609.
36 Y. Li, W. Zhou, H. Wang, L. Xie, Y. Liang, F. Wei, J.-C. Idrobo, S. J. Pennycook and H. Dai, *Nat. Nanotechnol.*, 2012, **7**, 394–400.
37 Z. Wen, S. Ci, Y. Hou and J. Chen, *Angew. Chem. Int. Ed.*, 2014, **53**, 6496–6500.
38 F. J. Maldonado-Hódar, C. Moreno-Castilla, J. Rivera-Utrilla, Y. Hanzawa and Y. Yamada, *Langmuir*, 2000, **16**, 4367–4373.
39 S. C. Yan, Z. S. Li and Z. G. Zou, *Langmuir*, 2009, **25**, 10397–10401.
40 E. Proietti, F. Jaouen, M. Lefèvre, N. Larouche, J. Tian, J. Herranz and J.-P. Dodelet, *Nat. Commun.*, 2011, **2**, 416.
41 F. Jaouen, J. Herranz, M. Lefèvre, J.-P. Dodelet, U. I. Kramm, I. Herrmann, P. Bogdanoff, J. Maruyama, T. Nagaoka, A. Garsuch, J. R. Dahn, T. Olson, S. Pylypenko, P. Atanassov and E. A. Ustinov, *ACS Appl. Mater. Interfaces*, 2009, **1**, 1623–1639.
42 F. Jaouen, M. Lefèvre, J.-P. Dodelet and M. Cai, *J. Phys. Chem. B*, 2006, **110**, 5553–5558.
43 H. Hou, C. E. Banks, M. Jing, Y. Zhang and X. Ji, *Adv. Mater.*, 2015, **27**, 7861–7866.
44 H. Cui, J. Zheng, P. Yang, Y. Zhu, Z. Wang and Z. Zhu, *ACS Appl. Mater. Interfaces*, 2015, **7**, 11230–11238.
45 Y. Niwa, H. Kobayashi and T. Tsuchiya, *Inorg. Chem.*, 1974, **13**, 2891–2896.
46 D. Yu, Q. Zhang and L. Dai, *J. Am. Chem. Soc.*, 2010, **132**, 15127–15129.
47 C. A. Melendres, *J. Phys. Chem.*, 1980, **84**, 1936–1939.
48 C. Dominguez, F. J. Perez-Alonso, M. A. Salam, S. A. Al-Thabaiti, M. A. Pena, L. Barrio and S. Rojas, *J. Mater. Chem. A*, 2015, **3**, 24487–24494.
49 M. Piana, S. Catanorchi and H. Gasteiger, *ECS Trans.*, 2008, **16**, 2045–2055.
50 H. Meng, F. Jaouen, E. Proietti, M. Lefèvre and J.-P. Dodelet, *Electrochem. Commun.*, 2009, **11**, 1986–1989.
51 G. Wu, K. L. More, P. Xu, H.-L. Wang, M. Ferrandon, A. J. Kropf, D. J. Myers, S. Ma, C. M. Johnston and P. Zelenay, *Chem. Commun.*, 2013, **49**, 3291–3293.